

Emission-Line Eclipse Mapping of Velocity Fields in a Dwarf-Nova Accretion Disk

Makoto MAKITA

Department of Astronomy, Kyoto University, Sakyo-ku, Kyoto 606-8502

makoto@kusastro.kyoto-u.ac.jp

and

Shin MINESHIGE

Yukawa Institute for Theoretical Physics, Kyoto University, Sakyo-ku, Kyoto 606-8502

minesige@yukawa.kyoto-u.ac.jp

(Received 2002 February 21; accepted 2002 April 2)

Abstract

We propose a new method, *emission-line eclipse mapping*, to map the velocity fields of an accretion disk in position space. Quiescent dwarf novae usually exhibit double-peaked emission line profiles because of disk rotation. Since a part of a disk having a different line-of-sight velocity is successively obscured by a companion in eclipsing systems, they show time-varying line profiles. We calculated the time changes of the emission-line profiles, assuming Keplerian rotation fields ($v_\phi \propto r^{-1/2}$ with r being the distance from the disk center) and an emissivity distribution of $j \propto r^{-3/2}$. We, then, applied the usual eclipse mapping technique to the light curves at each of 12–24 wavelengths across the line center to map the region with the same line-of-sight velocity. The reconstructed images typically exhibit a ‘two-eye’ pattern for high line-of-sight velocities, and we can recover the relation, $v_\phi \propto d^{-1/2}$, on the assumption of an axisymmetric disk, where d is the separation between the two ‘eyes’. We will be able to probe the Keplerian rotation law, the most fundamental assumption adopted in many disk models, by high-speed spectroscopic observations with 8-m class telescopes.

Key words: accretion, accretion disks — binaries: close, eclipsing — novae, cataclysmic variables — methods: numerical — techniques: image processing

1. Introduction

It is widely recognized that accretion disks play principal roles in various objects, including protostars, cataclysmic variables (CVs), X-ray binaries (XBs), and active galactic nuclei. Among them, CVs are the most ideal objects for accretion-disk research for the following rea-

sons. They are composed of a mass-losing, Roche-lobe-filling late-type star and an accreting white dwarf, and their orbital periods typically range between 1.5 and 10 hr. Such timescales are very convenient for ground-based observations. They are numerous; in other words, there are many CVs in our neighborhood. Also, CVs are bright in optical bands and exhibit a variety of time variations, some of which are closely related to various accretion-disk processes. Unlike XBs, moreover, the irradiation flux from the central parts of the disk and from the central objects is not very large, which makes accretion physics much simpler than otherwise. Hence, CVs are useful laboratories to investigate accretion-disk physics. However, the size of the accretion disks in CVs is typically $\sim R_\odot$, which is too small to resolve with ordinary telescopes; that is, we always collect all of the photons emitted from the entire disk surface (except for some special cases of young stellar objects). To test the disk theory with observations, therefore, we are obliged to compare the results only in terms of the integrated values, which cannot uniquely constrain the spatial structure of accretion disks.

There exists, however, a novel method to indirectly ‘resolve’ the surface brightness distribution over the disk plane. That is eclipse mapping (Horne 1985, 1993), which makes use of the eclipse of high-inclination binary systems. Since a part of the disk is successively obscured by the secondary star during an eclipse, the eclipsing light curves contain information regarding the brightness distribution over the disk plane. We can reconstruct a two-dimensional (2D) brightness distribution from one-dimensional eclipse light curves based on the concept of the maximum entropy. [As for the case of quasars, one may use microlens events by stars in intervening galaxies (e.g., Yonehara et al. 1998), but this method is irrelevant here.] Similarly important is the technique of Doppler tomography (Marsh, Horne 1988). Since the line profiles reflect velocity fields within the binary systems, including those of the secondary star and the gas stream to the disk, we can map the line-emissivity distribution in two-dimensional velocity space by analyzing the line-profile variations during the course of the orbital motions. This method, however, provides no definite information regarding the velocity fields in position (real) space.

We, here, consider a third method, by combining the above two methods, to map *the velocity fields in position space over the disk plane*. The goal is to verify whether the disk rotation velocity (v_φ) simply obeys the Kepler’s law, $v_K = \sqrt{GM_1/r}$ (with M_1 and r being the mass of a compact object and the distance from the central object, respectively). Moreover, we may be able to detect deviations from Keplerian rotation due to spiral shock patterns (Sawada et al. 1986a, b) and/or non-negligible magnetic fields. Thus, we can say that mapping the disk velocity fields in position space is one of the most fundamental tests of the basic disk models. Nevertheless, nobody has yet completed such a method, to our best knowledge, partly because for that purpose we need to detect changes of emission-line profiles during eclipse (lasting only several tens of minutes), which requires an enormous amount of photons, too much to collect with 4-m class telescopes. Recently built 8-m class telescopes can do this job, however. In this

paper, we describe the basic methodology and a simple test to probe the disk velocity fields by using the eclipse of emission-line profiles during the quiescence of dwarf novae.

Note that an apparently similar method has been proposed by Vrielmann et al. (1995); however, no detailed description is available and here we present an independent, slightly different method of our own. In section 2, we give basic considerations and then present the adopted model assumptions and procedures. Next, we explain our calculations of model light curves, assuming Keplerian rotation velocity fields, and present the resultant one-dimensional velocity profile obtained by the proposed method in section 3. The final section is devoted to discussion.

2. Model and Procedure

2.1. Basic Considerations

Dwarf novae (DNe) are a subclass of CVs and are unique in showing repetitive outbursts. During the quiescent states between outbursts, DNe usually exhibit strong, double-peaked emission lines due to Doppler effects caused by disk rotation. Therefore, each line profile contains information about the disk velocity fields, although we cannot spatially resolve them. In eclipsing systems, however, a part of the disk, which has a different line-of-sight velocity, is successively obscured by a companion star, giving rise to time variations of the emission line profiles. We then apply the usual eclipse mapping technique to the radiation flux at each of multiple wavelengths across the line center to obtain the emissivity distribution of the region moving with the corresponding line-of-sight velocity on the 2D disk plane. With the radial emissivity distribution being specified, we are able to obtain the rotational velocity as a function of radius on the assumption of circular motion.

According to Horne and Marsh (1986) and Marsh and Horne (1988), who calculated and displayed the contours of the constant line-of-sight velocity ($v_{\text{l.o.s.}}$) on the disk plane and the corresponding wavelengths ($\delta\lambda/\lambda_0 = v_{\text{l.o.s.}}/c$ with λ_0 being the line center wavelength), the shapes of the contours are distinct for high and low line-of-sight velocities: The large- $v_{\text{l.o.s.}}$ contours exhibit ‘two-eye’ patterns and their separation increases with a decreasing line-of-sight velocity. The small- $v_{\text{l.o.s.}}$ contours, on the other hand, show more complex patterns similar to the shape of a dipole field. For a reference, we display the contours of the constant line-of-sight velocity in Keplerian rotation viewed at the binary phase 0.0 for the case of an inclination angle of $i = 80^\circ$ in figure 1. The critical velocity discriminating these two different patterns is given by $\pm v_\varphi(R_{\text{out}})\sin i$, with R_{out} being the radius of the outer edge of the disk, which corresponds to the wavelengths of the two (blue and red) peaks in the line profile. Since the large- $v_{\text{l.o.s.}}$ parts are much easier to deal with, we, here, aim to map the emissivity distribution of those parts. In other words, we focus on an analysis of the wing parts of the double-horned line profiles. Then, as mentioned above, the relation between the line-of-sight velocity and the separation

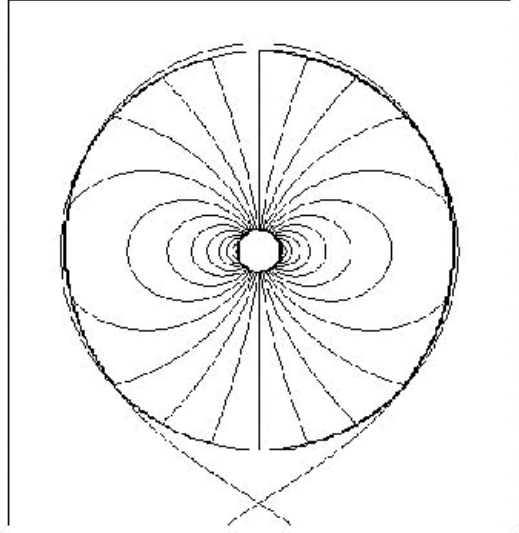


Fig. 1. Contours of the constant line-of-sight velocity on the disk plane for the case of an inclination of $i = 80^\circ$ and a mass ratio of $q = 0.5$. This picture corresponds to the case of $N = 12$, where N is the number of wavelength bins.

between the two ‘eyes’ (referred to as d) provides information regarding the disk rotational velocity fields on the axisymmetric assumption. Since i , M_1 , and other binary parameters are not usually precisely determined, we do not pay much attention to the absolute values of $v_{\text{l.o.s.}}$ but are concerned with the relative relationship (e.g., a power-law index, if represented as a power-law) between $v_{\text{l.o.s.}}$ and d .

2.2. Disk Model

We calculated the line-profile variations during an eclipse for a simple case and tested our method to see to what extent we can derive information regarding velocity fields. We considered a semi-detached binary system composed of a primary star with a mass of M_1 and a secondary star with a mass of M_2 . We assumed: (1) a geometrically thin accretion disk is formed around the primary, (2) disk materials are orbiting on the circular orbits around the primary with the Keplerian velocity, and (3) the secondary star fills its Roche lobe. In calculations, we set the binary separation, a , to be a unit of the length scale. We further assumed a line emissivity of

$$j(r) = \left(\frac{r}{R_{\text{in}}} \right)^{-\frac{3}{2}} \quad (1)$$

(see Horne, Saar 1991; Horne 1994) between the radius of the inner edge of the disk, $R_{\text{in}} = 0.05$, and that of the outer edge, $R_{\text{out}} = 0.5$ in units of binary separation, a . (If we perform Doppler tomography at the same time, it is not necessary to assume $j(r)$, since we can derive it on the assumption of the axisymmetric disk.)

As for the binary system parameters, we adopted a mass ratio of $q \equiv M_2/M_1 = 0.5$, a binary separation of $a = R_\odot$, and an inclination angle of $i = 80^\circ$. In physical units, the Keplerian rotation velocity is

$$v_K = \sqrt{\frac{GM_1}{r}} \sim 1000 \left(\frac{M_1}{M_\odot} \right)^{1/2} \left(\frac{r}{10^{10} \text{cm}} \right)^{-1/2} \text{ km s}^{-1}. \quad (2)$$

That is, we needed to cover velocity ranges of $v \simeq (1000\text{--}3000) \sin i \text{ km s}^{-1}$ for the radius range of $r \simeq 10^9\text{--}10^{10} \text{cm}$ and $M_1 \sim M_\odot$. Corresponding Doppler shifts are $\delta\lambda/\lambda_0 = v \sin i / c \simeq (0.003\text{--}0.01) \sin i$ (with c being the speed of light).

2.3. Procedure of the Emission-Line Eclipse Mapping

We divided the emission line profile into $N=12$ or 24 sections with a constant wavelength interval, $\Delta\lambda/\lambda_0 = 0.014/N$. We calculated the continuum flux with an equivalent width (EW) of 100\AA , and each line flux was normalized with this continuum flux. In the following, $F_{\text{cont}} = 1.0$ and $F_{\text{line}}(\lambda)$ refers to the normalized line flux with respect to F_{cont} .

For each section, an eclipse light curve was constructed from the binary phase $\phi = -0.15$ to $\phi = +0.15$ with 51 phase bins. We summed up the emission of the two sections (i.e. on the blue and red sides), which have the same absolute line-of-sight velocity, to increase the number of photons and normalized it with its maximum value. In some model, we only used either side of the emission profile, since that would be better when the line profile is highly asymmetric. Then, we made an eclipse map using the PRIDA code (Baptista, Steiner 1991, 1993) for each of N calculated light curves with different wavelengths. As for the default map, we, here, simply used an axisymmetric map (discussed later). We fixed the inclination angle to be $i = 80^\circ$.

3. Reconstructed Images and Velocity Fields

3.1. Basic Model

We first calculated the expected light curves based on the line-profile changes for the simple cases of $N = 12$ and 24; i.e., we supposed that 12 (or 24) light curves at 12 (24) different wavelengths are available. Figure 2 show the images of the eclipsed disk (left) and the calculated emission line profiles for the cases of $N = 12$ (middle) and for those of $N = 24$ (right), respectively, for five different binary phases; from the top, $\phi = -0.12, -0.06, 0.0, 0.06$, and 0.12 , respectively. Here, the binary phase of $\phi = 0$ corresponds to the mid-eclipse phase. Note that the binary rotates counterclockwise.

There are several features which deserve attention. First, most of the line profiles exhibit double peaks, and the wavelengths of the two peaks do not vary significantly (see, e.g., those in the first, third, and fifth rows). In contrast, the line wings are mostly missing in the third row because of the eclipse of the innermost part of the disk, which has large rotation velocities. Second, the line profiles before and after the eclipse of the central region (i.e., in the second

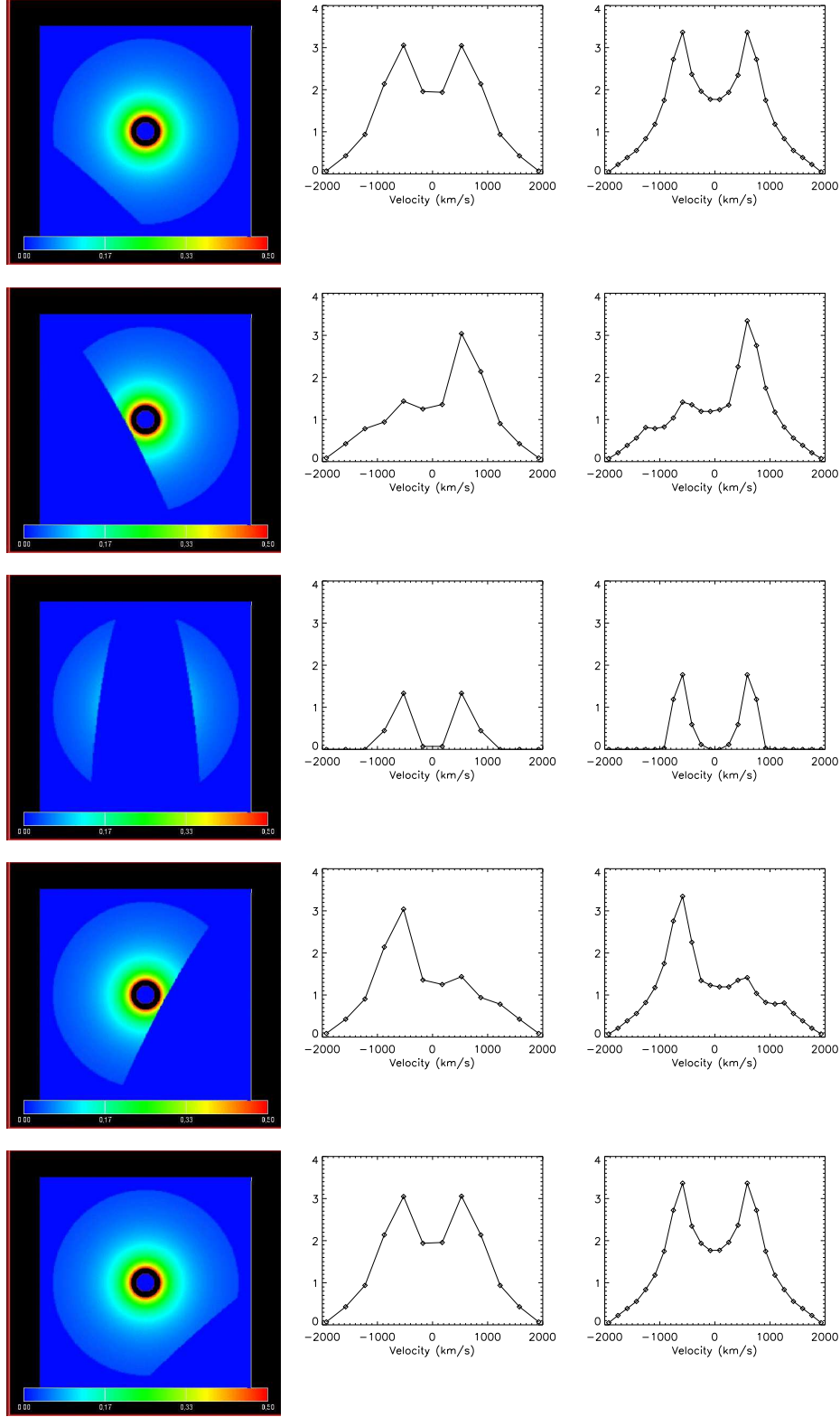


Fig. 2. Eclipsed disk images (left), emission line profiles $[F_{\text{line}}(\lambda)]$ for the case of 12 wavelength bins across the line profile (i.e. $N=12$; middle), and those of $N=24$ (right), respectively, for five different binary phases; from the top to bottom, $\phi = -0.12, -0.06, 0.00, 0.06$ and 0.12 , respectively. The disk is seen by a viewer at the bottom of the page.

and fourth rows) still show two peaks at the same wavelengths as those in the other panels. In addition, one more weak peak is found in the right panel with finer wavelength bins ($N = 24$). Such subtle spectral-line changes are important for successful emission-line mapping, thus a huge number of photons are required. Obviously, double-horned line profiles are smoother in $N = 24$ than those in $N = 12$. Finally, line profiles at one phase (say, $\phi = \phi_0$) and those at another phase with opposite sign ($\phi = -\phi_0$) are exactly symmetric with respect to the line center. Thus, the light curves at one wavelength (say, at $\lambda_0 + \Delta\lambda$) are exactly symmetric in time with respect to the minimum with those at another wavelength at $\lambda_0 - \Delta\lambda$. This may not be the case in realistic situations because of the finite thickness effects and possible warps in the disk.

We next display in figure 3 the original maps (left), synthetic light curves (middle left), and the reconstructed maps obtained by using both of the red and blue sides of the line profiles (middle right), and those reconstructed by using only the red side (right), respectively. We used $N = 12$ wavelength bins for these mappings. Since the light variations of the red and blue sides are symmetric, as mentioned above, we simply summed up the two contributions in the light curves to acquire good photon statistics. The middle panels show a diversity of light curves at different wavelengths. The upper two panels representing the cases of high velocities show similar variations to those of the continuum, but with a shorter duration, since they have no complicated shape of the emission region. As we look downward, the corresponding velocities decrease and the images start to show a complex pattern. Accordingly, the light curves are changed in a complex fashion. Especially, the light curves at the minimum is nearly flat in the upper three rows (although the duration of the minimum decreases downward), which contrasts rather complex variations in other two rows. This feature suggests that the high-velocity parts of the line-profile variations seem to be easier to derive any concrete information.

Eclipse maps are constructed with 21×21 grids. The constructed maps displayed in the middle right panels of the upper two rows show the characteristic ‘two-eye’ patterns, which recover the qualitative features of the original maps. In the lower three rows representing the cases of low line-of-sight velocities, in contrast, the constructed images (depicted in the middle right panels) hardly recover the original map. This is because we used an axisymmetric default image in the reconstruction, whereas the line emission profile of the original map is far from being axisymmetric.

To fix such a problem, we only use the red side of the line profile and show the results in the right panels of the lower three rows in figure 3. Interestingly, the right panels can recover a part of the eclipsed region on one side more clearly. In the third row, especially, the right panel shows a clear eye-shaped pattern, which is not seen in the middle right one. This, therefore, suggests that we are able to obtain the information of velocity for the case of $v_{\text{l.o.s.}} = 700\text{--}1050$ km s $^{-1}$ even in $N = 12$.

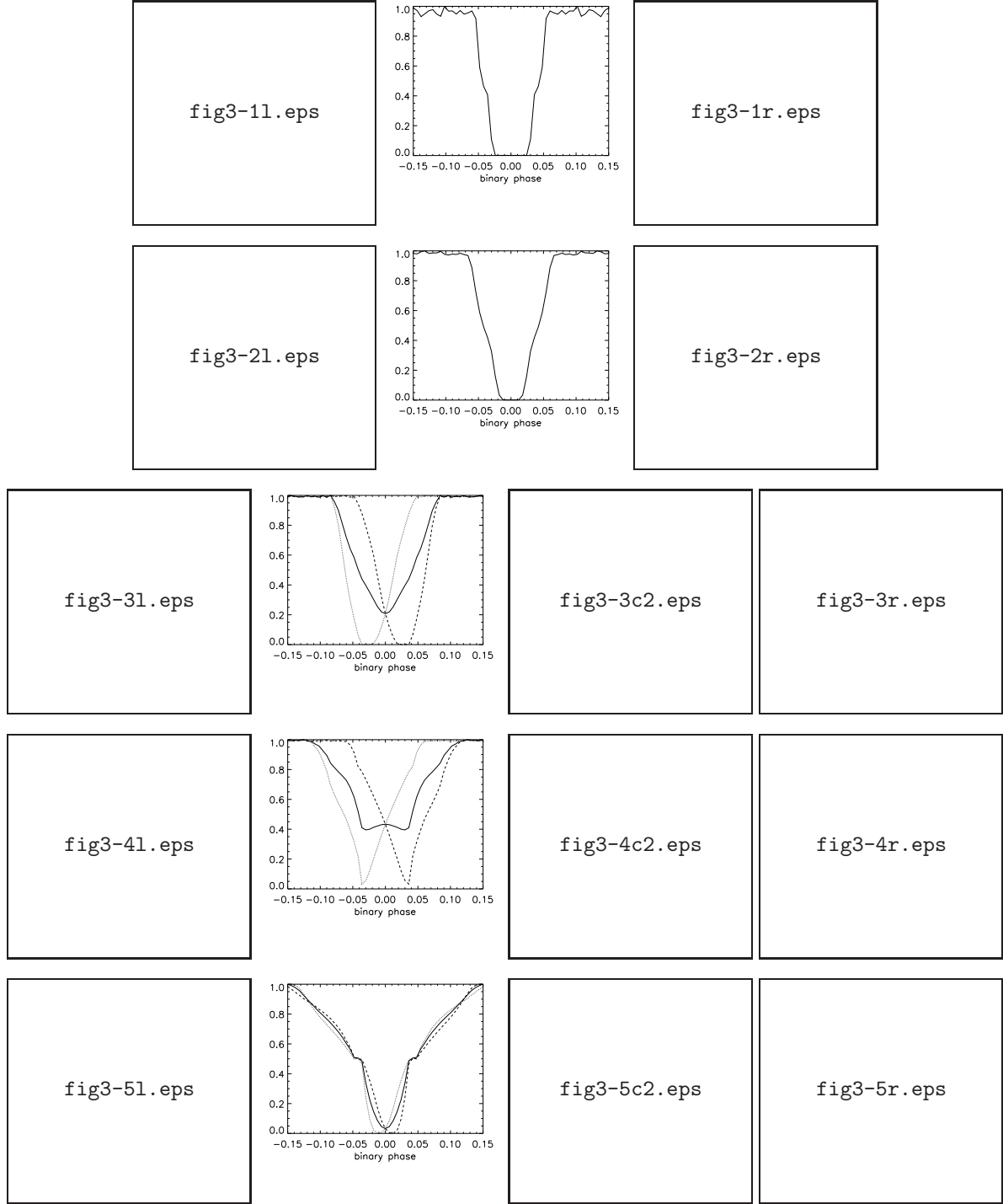


Fig. 3. Original emissivity maps (left panels), synthetic light curves (middle left), and the reconstructed maps (middle right) for the cases of $N = 12$. The right panels in the lower three rows are reconstructed maps derived solely from the red side of the line profiles. Each row of the panels represents, from the top to bottom, the line-of-sight velocities of $v_{l.o.s.} = 1400\text{--}1750, 1050\text{--}1400, 700\text{--}1050, 350\text{--}700$, and $0\text{--}350$ km s^{-1} , respectively. In the light curves, the solid, dotted and dashed lines show those of the sum of the blue and red sides, blue, and red side, respectively. The disk is seen by a viewer at the bottom of the page.

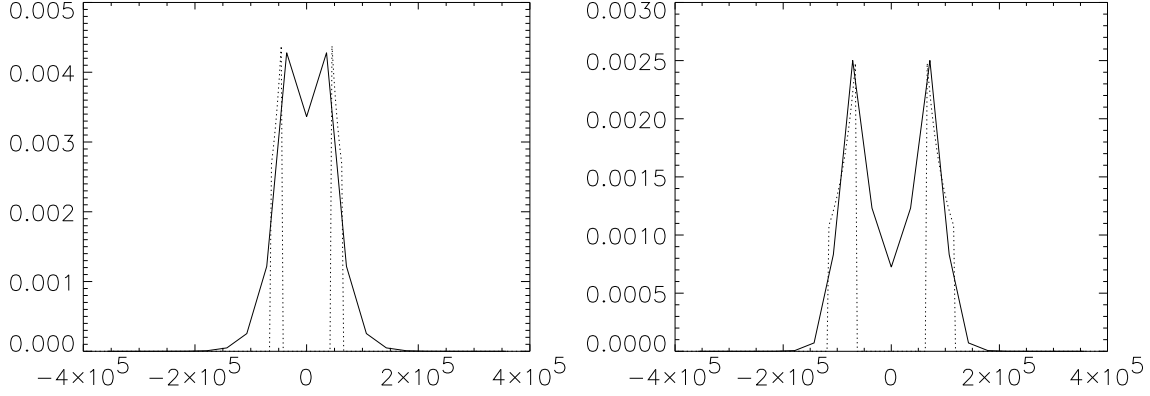


Fig. 4. One-dimensional distributions of the original (dotted) and the reconstructed (solid) line emissivity profiles along the x -axis for $v_{\text{l.o.s.}} = 1400\text{--}1750 \text{ km s}^{-1}$ (left panels) and $1050\text{--}1400 \text{ km s}^{-1}$ (right panels), respectively. The flux of the eclipse maps is multiplied by 25.

3.2. Line Emissivity Distributions

To see line-emissivity distributions more quantitatively, we illustrate in figure 4 cross-sectional views of the emissivity profile along the x -axis. The emissivity profiles of the original map are illustrated by the dotted lines, while those of the reconstructed map are by the solid lines. Although the reconstructed one shows a broader distribution, the peak wavelengths do not differ much in both panels. This figure confirms that the spatial positions of the two ‘eyes’ in the reconstructed images are to good accuracy equal to those of the original ones. That is, the reconstruction is quite successful at least as long as data of ~ 50 observational runs over one eclipse are available with good photon statistics.

3.3. Models with Large Number of Grids

In figure 5, we present only the eclipse maps which show the characteristic ‘two-eye’ pattern for the case of $N = 24$. The left panels are for 21×21 grids, as in figure 3, while the right panels show finer maps with 41×41 grids. The data for $v_{\text{l.o.s.}} = 1575\text{--}1750 \text{ km s}^{-1}$ are not shown, since no convergence is reached in the latter case. Comparing the left panels with the right ones, we notice that finer maps represent more circular images. However, the positions of two ‘eyes’ do not differ significantly.

3.4. The Rotation Law

Finally, we calculated, for each line-of-sight velocity, the distance from the primary star in the real space based on the separation between the two ‘eyes’ on the reconstructed image; the result is plotted in figure 6. As is clear, the reconstructed line-of-sight velocities are roughly on the straight, dotted line with a slope in proportion to $d^{-1/2}$. That is, our proposed method is feasible to reconstruct Keplerian velocity fields, as long as good photon statistics is achieved.

To see how observational errors affect our results, we repeated the same procedure, but



Fig. 5. Reconstructed maps for the case of $N = 24$, left panels show models with 21×21 grids, while the right ones show those with 41×41 grids. The line-of-sight velocities are, from top to bottom, $v_{\text{l.o.s.}} = 1750\text{--}1925$, $1400\text{--}1575$, $1225\text{--}1400$, and $875\text{--}1050 \text{ km s}^{-1}$, respectively. The disk is seen by a viewer at the bottom of the page.

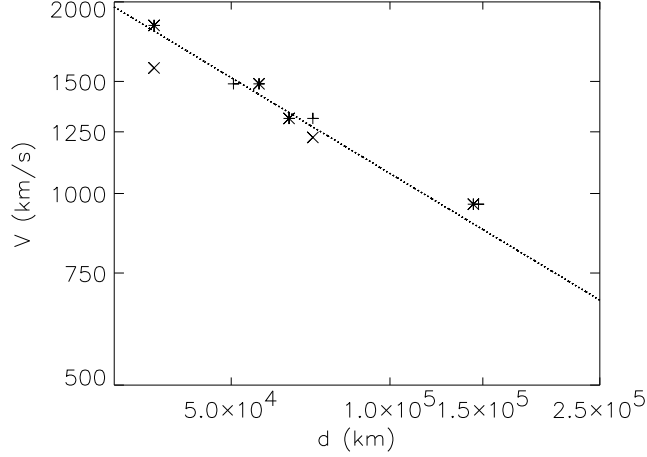


Fig. 6. Line-of-sight velocities obtained by the image reconstruction technique as functions of the distance from the primary star. The results for the case of $N = 12$ are indicated by ‘+’, while those of $N = 24$ are by ‘x’, respectively, both obtained with 21×21 grids. ‘*’ also shows the results for the case of $N = 24$ and 41×41 grids. For a comparison, we depict the Keplerian velocity relation, $v \propto r^{-1/2}$, by the dotted line.

added random errors in calculating the light curves at each wavelength. Namely, we calculate the observable line flux, $F_{\text{line}}^{\text{obs}}$, from the theoretically modeled flux, $F_{\text{line}}^{\text{model}}$ according to the following steps:

1. $F_{\text{tot}}^{\text{model}}(\lambda) \equiv F_{\text{line}}^{\text{model}}(\lambda) + F_{\text{cont}}$,
2. $F_{\text{tot}}^{\text{obs}}(\lambda) = F_{\text{tot}}^{\text{model}}(\lambda) + \epsilon(S/N)^{-1} \sqrt{F_{\text{tot}}^{\text{model}}(\lambda)}$,
3. $F_{\text{line}}^{\text{obs}}(\lambda) \equiv F_{\text{tot}}^{\text{obs}}(\lambda) - F_{\text{cont}}$.

Here, ϵ represents the Gaussian noise (with the mean being zero and the standard deviation being unity); the amount of random variations is given by the signal-to-noise ratio (S/N). Note that we set $F_{\text{cont}} = 1.0$, and $F_{\text{line}}^{\text{model}}$ was calculated so as to give an equivalent width of 100\AA (see subsection 2.3).

We calculated the cases of $S/N = 10, 20$, and 50 as representative examples. We found that in some cases convergence is not always guaranteed in the eclipse mapping process, because the light curve is not symmetric when random errors are added. Nevertheless, we expected good results, even if we solely consider the cases with successful reconstruction. Figure 7 presents the results of the relatively noisy cases of $S/N = 10$. The number of wavelength bins is $N = 24$. It is impressive to see that the Keplerian relation is roughly reproduced, although we used only those results which have the clear ‘eye’ pattern. These results demonstrate that our proposed method is powerful even for the case of $S/N = 10$, as long as the reconstructed eclipse map displays the ‘eye’ pattern.

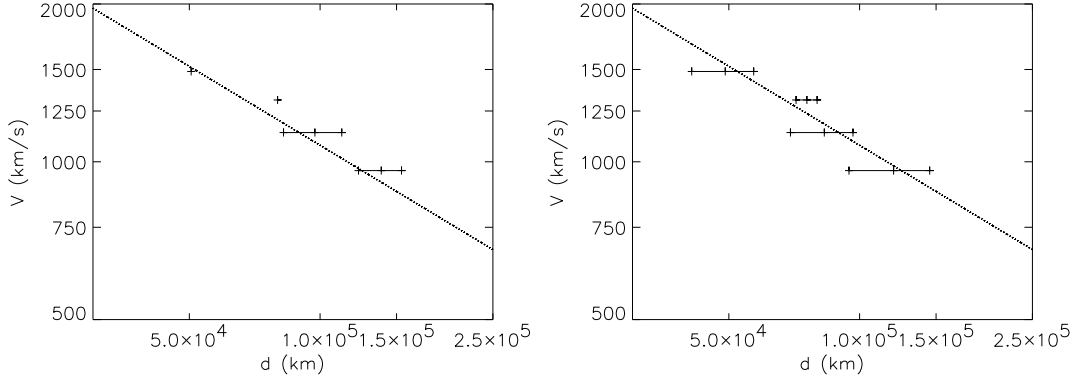


Fig. 7. Effect of noise in the case of $N(\text{wavelength bins}) = 24$. In the case of $S/N = 10$, the left panel shows the result with 21×21 grids for the reconstruction and the right panel does the one with 41×41 grids. For a comparison, we also depict the Keplerian velocity relation, $v \propto r^{-1/2}$, with the dotted line.

4. Discussion

We propose *emission-line eclipse mapping* to map the velocity fields in an accretion disk. We studied the feasibility of emission-line eclipse mapping using model simulations. Our results show that those regions having high line-of-sight velocities can be precisely reconstructed, while the low line-of-sight regions are not, as long as an axisymmetric default image is used. These reconstructed maps of high line-of-sight velocities show the characteristic ‘two-eye’ pattern. The corresponding line-of-sight velocity recovers the originally adopted relation, which is proportional to $d^{-0.5}$. It means that this method is a potentially useful tool to probe the Keplerian disk rotation from observations of the line-profile variations.

Although the Keplerian rotation is a fundamental assumption in constructing the so-called standard disk model, it is not always trivial from a theoretical point of view. For example, a rather hot accretion flow, called ADAF (advection-dominated accretion flow), predicts sub-Keplerian rotation (Kato et al. 1998); i.e., $v_\phi < v_K$. In addition, the velocity fields are affected by the presence of large-scale magnetic fields and/or spiral patterns, which will produce deviations from the exact Keplerian velocity of the order of $\delta v/v_K \sim v_A/v_K \sim c_s/v_K \sim H/R \simeq 1/30$ (where v_A and c_s are the Alfvén velocity and the sound velocity, respectively, and H/R is the aspect ratio of the disk). To detect such small effects we need to collect an enormous number of photons, which are unavailable at the present. Thus, we should await innovations of the observation technique.

For successful reconstructions, we need rather frequent observations over the eclipse periods. Only 8-m class telescopes, such as Subaru, can meet this requirement, which is underway. The next issues are to improve the current method so as to minimize the total observing times by modifying the default images and to perform observations studies (e.g., Vriellmann et al. 1995).

We are grateful to Taichi Kato and Raymundo Baptista for useful discussion and helpful comments. The author (M. M.) also thanks Makoto Uemura for his advice on using PRIDA code. This work was supported in part by the Grants-in Aid of the Ministry of Education, Culture, Sports, Science and Technology (13640238, SM).

References

- Baptista, R., & Steiner, J. E. 1991, *A&A*, 249, 284
Baptista, R., & Steiner, J. E. 1993, *A&A*, 277, 331
Horne, K. 1985, *MNRAS*, 213, 129
Horne, K. 1993, in *Accretion Disks in Compact Stellar Systems*, ed. J. C. Wheeler (Singapore: World Scientific), 117
Horne, K. 1994, in *Theory of Accretion Disks – 2*, ed. W. J. Duschl, J. Frank, F. Meyer, E. Meyer-Hofmeister, & W. M. Tscharnuter (Dordrecht: Kluwer Academic Publishers), 77
Horne, K., & Marsh, T. R. 1986, *MNRAS*, 218, 761
Horne, K., & Saar, S. H. 1991, *ApJ*, 374, L55
Kato, S., Fukue, J., & Mineshige, S. 1998, *Black-Hole Accretion Disks* (Kyoto: Kyoto Univ. Press)
Marsh, T. R., & Horne, K. 1988, *MNRAS*, 235, 269
Sawada, K., Matsuda, T., & Hachisu, I. 1986, *MNRAS*, 219, 75
Sawada, K., Matsuda, T., & Hachisu, I. 1986, *MNRAS*, 221, 679
Yonehara, A., Mineshige, S., Manmoto, T., Fukue, J., Umemura, M., & Turner, E. L. 1998 *ApJ*, 501, L41 (Erratum 511, L65)
Vrielmann, S., Horne, K., & Baptista, R. 1995, in *Cataclysmic Variables*, ed. A. Bianchini, M. della Valle, & M. Orio (Dordrecht: Kluwer Academic Publishers), 376

This figure "fig3-11.jpg" is available in "jpg" format from:

<http://arxiv.org/ps/astro-ph/0204363v2>

This figure "fig3-1r.jpg" is available in "jpg" format from:

<http://arxiv.org/ps/astro-ph/0204363v2>

This figure "fig5-11.jpg" is available in "jpg" format from:

<http://arxiv.org/ps/astro-ph/0204363v2>

This figure "fig5-1r.jpg" is available in "jpg" format from:

<http://arxiv.org/ps/astro-ph/0204363v2>

This figure "fig3-2l.jpg" is available in "jpg" format from:

<http://arxiv.org/ps/astro-ph/0204363v2>

This figure "fig3-2r.jpg" is available in "jpg" format from:

<http://arxiv.org/ps/astro-ph/0204363v2>

This figure "fig3-3c2.jpg" is available in "jpg" format from:

<http://arxiv.org/ps/astro-ph/0204363v2>

This figure "fig3-4c2.jpg" is available in "jpg" format from:

<http://arxiv.org/ps/astro-ph/0204363v2>

This figure "fig3-5c2.jpg" is available in "jpg" format from:

<http://arxiv.org/ps/astro-ph/0204363v2>

This figure "fig5-2l.jpg" is available in "jpg" format from:

<http://arxiv.org/ps/astro-ph/0204363v2>

This figure "fig5-2r.jpg" is available in "jpg" format from:

<http://arxiv.org/ps/astro-ph/0204363v2>

This figure "fig3-3l.jpg" is available in "jpg" format from:

<http://arxiv.org/ps/astro-ph/0204363v2>

This figure "fig3-3r.jpg" is available in "jpg" format from:

<http://arxiv.org/ps/astro-ph/0204363v2>

This figure "fig5-3l.jpg" is available in "jpg" format from:

<http://arxiv.org/ps/astro-ph/0204363v2>

This figure "fig5-3r.jpg" is available in "jpg" format from:

<http://arxiv.org/ps/astro-ph/0204363v2>

This figure "fig3-4l.jpg" is available in "jpg" format from:

<http://arxiv.org/ps/astro-ph/0204363v2>

This figure "fig3-4r.jpg" is available in "jpg" format from:

<http://arxiv.org/ps/astro-ph/0204363v2>

This figure "fig5-4l.jpg" is available in "jpg" format from:

<http://arxiv.org/ps/astro-ph/0204363v2>

This figure "fig5-4r.jpg" is available in "jpg" format from:

<http://arxiv.org/ps/astro-ph/0204363v2>

This figure "fig3-5l.jpg" is available in "jpg" format from:

<http://arxiv.org/ps/astro-ph/0204363v2>

This figure "fig3-5r.jpg" is available in "jpg" format from:

<http://arxiv.org/ps/astro-ph/0204363v2>